Broadband locally resonant band gaps in periodic beam structures with embedded acoustic black holes

Liling Tang and Li Cheng

Broadband locally resonant band gaps in periodic beam structures with embedded acoustic black holes

Liling Tang and Li Cheng[a]
Department of Mechanical Engineering, The Hong Kong Polytechnic University, Hung Hom, Kowloon, Hong Kong

The Acoustic Black Hole (ABH) effect can be used to effectively reduce structural vibrations by trapping flexural waves in a thin-walled structure with a power-law thickness variation. In the present study, we used a wavelet-decomposed energy method to investigate an Euler-Bernoulli beam embedded with multiple ABHs. Broadband transmission attenuation bands at relatively low frequencies are observed in a beam containing only a few ABH elements. To explain the underlying phenomena, an infinite structure with periodic ABH elements is analyzed. Numerical results show that the periodic boundary conditions in terms of displacement and rotational slope of a unit cell, based on the finite model, are sufficient to describe the band structures, without requiring full treatment of the entire infinite structure. This provides an efficient and flexible means to predict, and eventually optimize, the band structure based on a single element. Meanwhile, the ABH-induced locally resonant band gaps coincide with the attenuation bands observed in the finite beams. Because of the unique ABH feature, the proposed beam requires only a small number of elements to obtain broad attenuation bands, which offers great potential for vibrational isolation applications and wave filter designs in beam structures. *Published by AIP Publishing.*
[http://dx.doi.org/10.1063/1.4983459]

I. INTRODUCTION

The Acoustic Black Hole (ABH) phenomenon has been attracting increasing attention in recent years as a promising method to passively control vibrations[1–7] by manipulating bending wave propagation in a thin-walled structure with a thickness tailored according to a power-law variation $h(x) = \varepsilon x^m$ ($m \geq 2$).[1,8] In the ideal scenario, the phase and group velocities of the bending waves gradually reduce to zero as the thickness diminishes,[8] resulting in zero wave reflection at the tip of the tapered area. In practice, however, a truncated tip thickness always exists. However, the inevitable wave reflections and compressed high amplitude waves near the tip can be effectively absorbed by applying a small amount of damping materials.[1,2]

Intensive ABH research has covered various aspects of both 1D and 2D structures in recent years. The effectiveness of using a single ABH element for attenuating bending vibrations has been demonstrated in various theoretical and experimental studies. Semi-infinite 1-D structures have been extensively investigated using models such as the geometrical acoustic approach[1,9] and the impedance method.[10] These studies reveal insight into the dominant wave propagation phenomena, such as the reduction in the reflection coefficient of flexural waves when the frequency increases. For 1-D structures of finite size, the ABH effect has also been observed both theoretically[11] and experimentally,[5,12] except for cases where energy localization takes place, which results in loss of the ABH effect.[13] Meanwhile, the use of different

thickness profiles was also exploited for both 1D[14–16] and 2D configurations.[17]

The major flaw of a single ABH element is that, although ABH effects start to appear above a certain frequency when local ABH dynamics are cut-on (referred to as the cut-on phenomenon[19]), systematic broadband ABH effects can only be achieved above a much higher frequency, referred to as the characteristic frequency (to be defined later in the paper) when the incoming wavelength becomes equal or less than the geometrical characteristic dimension of the ABH element. Embedding multiple ABHs can, to some extent, improve the low frequency performance without increasing the ABH dimension,[18] with applications extended for sound radiation.[19] Existing studies on multiple ABHs[18–21] are mostly based on experiment and the Finite Element Method. These studies show the ABH effect on wave propagation characteristics. However, the possible accumulated ABH effect and wave filter effect induced by multiple ABHs were not chosen to be the main focus of the discussions.

The advent of acoustic metamaterials, exemplified by the Phononic Crystals (PCs), gives new impetus to revisit the above issue. As one of the most attractive physical properties of the PCs, band gaps[22–25] can be generated, mainly through two physical mechanisms: Bragg scattering or local resonances.[26–30] The former leads to broad band gaps at subwavelength scales compared with the lattice constant to ensure destructive interferences. Therefore, to attenuate low frequency and long wavelength waves, the unit cell needs to be prohibitively large. Meanwhile, a large number of elements are needed to achieve broad band gaps. These limitations can be overcome using locally resonant band gaps by attaching local resonators, but the gaps are usually narrow. These

[a]Author to whom correspondence should be addressed: li.cheng@polyu.edu.hk.

two types of band gaps are difficult to conciliate. In addition, the demanding fabrication process and numerous interfaces required by conventional PCs also hamper the practical applications of the PCs. An interesting question is whether broad band gaps could be achieved at low frequencies through ABH effects by using a small number of ABH elements without attaching additional elements and creating multiple interfaces. If achievable, how can simulation and design serve to predict this behavior. This constitutes the main motivation of the present work. To the best of our knowledge, there is only one paper dealing with an infinite 2D ABH lattice.[31] The inspiring work clearly shows the dispersion properties of the structure without absolute band gaps, due to the multiple and complex wave travel paths. It is therefore interesting to revisit this issue in 1D configuration.

In this paper, we first investigate an Euler-Bernoulli beam containing multiple ABHs using a wavelet-decomposed energy method[11,13,14] in part II. Analyses are performed in terms of vibrational energy distributions and transmissions. Then, to illustrate and explain the physical phenomena arising from multiple ABHs, the wavelet-decomposed energy model is expanded to deal with an infinite periodic structure with ABHs in part III. The model is verified and the comparison between infinite and finite structures is made thereafter. Meanwhile, the ABH parameters are analyzed to achieve broader band gaps.

II. FINITE STRUCTURES WITH MULTIPLE ABHs

A. Theoretical model

A wavelet-decomposed and energy-based model[11] is used to investigate a structure of finite size with multiple ABHs, as shown in Fig. 1. The tapered ABH parts can be covered by thin damping layers. The thickness profile takes the form $h(x) = \varepsilon x^m + h_0$, as shown in Fig. 1(b). Artificial translational and rotational springs, of distributed stiffness K and Q, can be adjusted to achieve various boundary conditions. The damping of both the beam and the damping layer is taken into account within the complex Young's modulus E, i.e., $E = E(1 + i\eta)$, where η is the damping loss factor, to be assigned different values for the beam and the damping layer. Based on the Euler-Bernoulli beam theory, the displacement field of the beam and the damping layer is expressed as $\{u, w\} = \left\{ -z\frac{\partial w}{\partial x}, w(x,t) \right\}$. Taking the wavelength fluctuation along the beam into account, Mexican Hat Wavelets (MHW) $\varphi_{i,s}(x)$[32,33] are chosen to expand the flexural displacement w as[11]
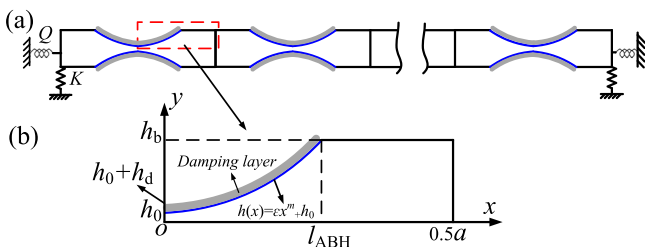

$$w(x,t) = \sum_{i=0}^{m} \sum_{s} a_{i,s}(t)\varphi_{i,s}(x) \tag{1}$$

with $\varphi_{i,s}(x) = \frac{2}{\sqrt{3}}\pi^{-\frac{1}{4}}2^{i/2}\left[1 - (2^i x - s)^2\right]e^{-\frac{(2^i x - s)^2}{2}}$.

The Lagrangian of the system is expressed as

$$L = E_k - E_p + W, \tag{2}$$

where E_k denotes the kinetic energy of the system; E_p is the potential energy; and W is the work done by the excitation force. They can be obtained, respectively, by

$$E_k = \frac{1}{2}\int \rho \left(\frac{\partial w}{\partial t}\right)^2 dV, \tag{3}$$

$$E_p = \frac{1}{2}\int EI(x)\left(\frac{\partial^2 w}{\partial x^2}\right)^2 dx + \frac{1}{2}Kw(x_{b4}, t)^2$$
$$+ \frac{1}{2}Q\left(\frac{\partial w(x_{b4}, t)}{\partial x}\right)^2, \tag{4}$$

$$W = f(t)w(x_f, t). \tag{5}$$

Using Lagrange's equations $\frac{d}{dt}\left(\frac{\partial L}{\partial \dot{a}_{i,s}(t)}\right) - \frac{\partial L}{\partial a_{i,s}(t)} = 0$ and simplifying the equations in the harmonic regime, one can get the vibration response by solving the following matrix equation:

$$[\mathbf{K} - \omega^2 \mathbf{M}]\mathbf{A} = \mathbf{F}, \tag{6}$$

where $\mathbf{K}$ and $\mathbf{M}$ are, respectively, the stiffness matrix and mass matrix; $\mathbf{A}$ and $\mathbf{F}$ are the vectors of the response and the excitation force, respectively. Setting the force vector in Eq. (6) to zero leads to the following eigenvalue equation:

$$\mathbf{M}^{-1}\mathbf{K}\mathbf{A} = \omega^2 \mathbf{A}, \tag{7}$$

which yields the natural frequencies and the corresponding mode shapes.

B. Illustration of Multiple ABH effects

As a numerical example, consider three free-free beams containing one, two, and three identical ABH elements, respectively. An entirely uniform beam, having the same thickness h_b and the same total length as the beam with three ABHs, is also included as a reference. The material and geometrical parameters are tabulated in Table I. A unit excitation force is applied at the free end of the beam, while the receiving point is placed at the other free end.

TABLE I. Material and geometrical parameters.

	Beam	Damping layers
Material parameters	$E_b = 210\,\text{GPa}$	$E_d = 5\,\text{GPa}$
	$\rho_b = 7800\,\text{kg/m}^3$	$\rho_d = 950\,\text{kg/m}^3$
	$\eta_b = 0.001$	$\eta_d = 0.1$
Geometrical parameters	$h_b = 0.32\,\text{cm}$	$h_0 = 0.02\,\text{cm}$
	$l_{\text{ABH}} = 2\,\text{cm}$	$a = 8\,\text{cm}$

FIG. 1. Sketch of (a) an Euler-Bernoulli beam with multiple ABHs and (b) the thickness profile.
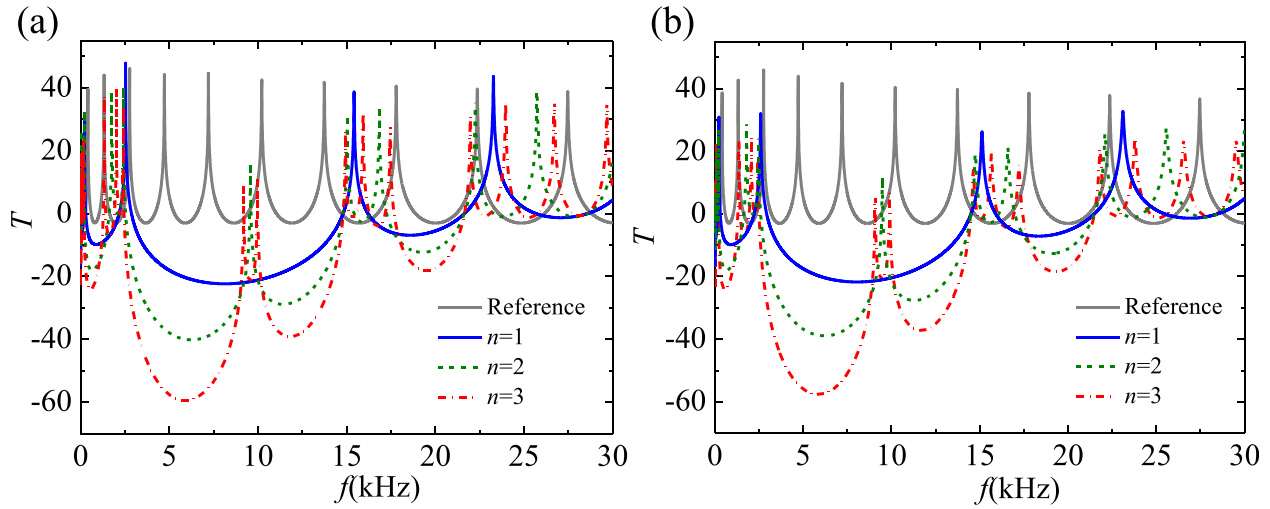
FIG. 2. Comparisons of vibration transmission involving beams with one, two, and three ABHs and the uniform reference beam: (a) with no damping layers applied and (b) with damping layers applied for $h_d = 0.02$ cm.

Figure 2(a) compares the vibration transmission of the three ABH beams with that of the reference beam without damping layers. The vibration transmission is defined as $20 \log \frac{w_{out}}{w_{in}}$, in which w_{in} is the input displacement at the excitation point and w_{out} is the output displacement at the receiving point. The vibration transmission of the beams with ABHs is significantly reduced in four broad frequency bands, 150–850 Hz, 2.1–8.8 kHz, 10.4–14.8 kHz, and 18.3–21.6 kHz, which can loosely be referred to as "attenuation bands" (Comparisons of these attenuation bands with the "band gaps" used in infinite structures will be performed at a later stage). Meanwhile, transmission reduces quite significantly as the number of ABHs increases. The minimum transmission reaches nearly −60 dB when three ABH elements are present. This observation suggests that, compared with the uniform beam, ABH elements act as efficient vibration isolators at specific frequencies even in the absence of the damping layers. The transmission curves are compared again in Fig. 2(b) for samples with damping layers applied over the ABH sections and the corresponding regions of the uniform reference beam. The damping layers show little influence on the attenuation bands in terms of both frequency distribution and attenuation intensity. However, energy concentration in the ABH section from the ABH effect leads to significantly reduced transmission of the beam with ABHs at the resonant frequencies, in agreement with the common understanding on the conventional ABH structures. As expected, this reduction is also increased with the number of ABH elements.

The displacement distribution at 5.8 kHz (roughly the trough of the second attenuation band) is compared in Fig. 3 for different beams with damping layers to examine what happens inside the attenuation bands. As can be seen, for the uniform reference beam, the vibration is fairly balanced along the entire beam span; with only one ABH element, the vibration is mainly concentrated on the ABH part, while the vibration energy is attenuated to some extent at the receiving point of the uniform part. With additional ABH elements, the wave is further attenuated when passing through each

ABH, resulting in negligible vibration towards the end of the uniform region for the beam with three ABH elements.

Focusing now on the beam with three ABHs with damping layers, its energy and displacement distribution along the beam span is further illustrated in Fig. 4. Fig. 4(a) shows the energy ratio $\Gamma (\Gamma = 10 \log \frac{\langle V^2 \rangle_{ABH}}{\langle V^2 \rangle_{Unif}})$ between each ABH part and the uniform part in terms of the averaged quadratic velocity with A1 denoting the ABH part closest to the force input. It can be seen that the energy is mainly trapped in the first ABH portion, adjacent to the force excitation, while less and less energy propagates to the subsequent ABH elements within the attenuation bands, as shown in Fig. 2. At other frequencies, however, the energy distribution among different ABHs is fairly balanced among different portions of the beam. This phenomenon can be substantiated by the displacement distribution at two representative frequencies as shown in Fig. 4(b). At 5.8 kHz in the second attenuation band with the lowest transmission (as also shown in Fig. 3), the vibration level is significantly suppressed after the wave passes through the first ABH, part A1, and the remaining vibration is almost negligible, especially for the last uniform part past the third ABH element, A3. However, at 25 kHz
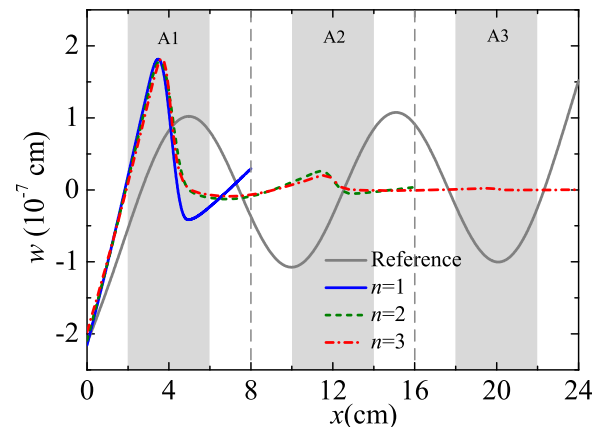

FIG. 3. Displacement distribution at 5.8 kHz for different beams with A1 denoting the ABH part closest to the point excitation.
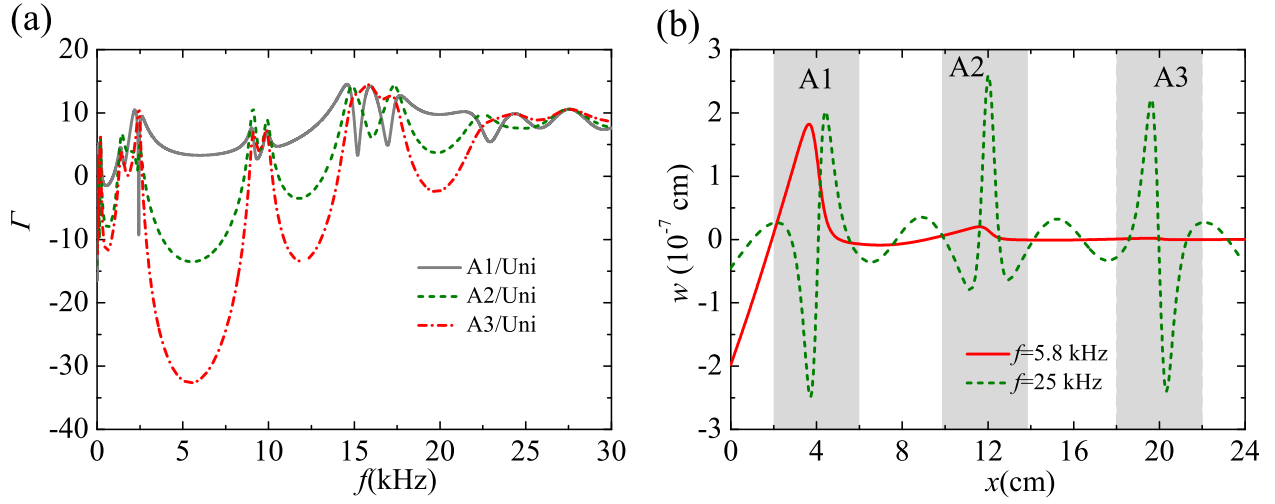
FIG. 4. (a) Energy ratio between the ABH part and the uniform part, with A1 denoting the ABH part closest to the excitation point, and (b) displacement distribution at 5.8 and 25 kHz. The shadow areas denote the three ABH regions.

beyond the fourth attenuation bands, the wave is compressed within the three ABH regions with the vibration amplitude greatly amplified compared with that of the remaining uniform part. Clearly, the vibration of the uniform part is reduced because of the ABH effect, but the displacement level within each ABH area remains comparable.

In conclusion, numerical simulations show the existence of the attenuation bands, within which significant wave attenuation can be achieved using a small number of ABH elements. Apparently they appear at relatively low frequencies, typically before a so-called "characteristic frequency f_c" which can be defined as $f_c = \frac{\pi h_b}{l^2_{ABH}} \sqrt{\frac{E_b}{12\rho_b}}$. Above this frequency, the incoming wavelength starts to be equal to or less than the geometrical characteristic dimension of the ABH element,[14,19] which is 16731 Hz in the present case. This frequency range can be loosely called mid-to-high frequencies. Contrary to the structure with a single ABH element where waves are systematically attenuated only after the characteristic frequency,[14] the structure with multiple ABHs brings new perspective to the wave attenuation.

III. INFINITE PERIODIC STRUCTURE MODEL

To better explain the physical phenomena observed from the above analyses with multiple ABHs, the wavelet-decomposed energy method is expanded to investigate an infinite lattice with periodic ABH cells, as shown in Fig. 5.

The flexural displacement w is again expanded using Mexican Hat Wavelets as in Eq. (1). The Lagrangian of the system is written as the sum of Lagrangians of every unit cell
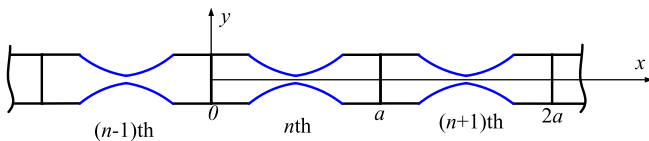

FIG. 5. Sketch of an infinite Euler-Bernoulli beam with periodic ABH cells with a lattice constant a.

$$L = \sum_{n=-\infty}^{+\infty} L_n = \sum_{n=-\infty}^{+\infty} E_{nk} - E_{np}, \quad (8)$$

where E_{nk} and E_{np} are, respectively, the kinetic energy and the potential energy of the nth unit-cell, expressed as

$$E_{nk} = \frac{1}{2} \int \rho \left(\frac{\partial w_n(x)}{\partial t} \right)^2 dV, \quad E_{np} = \frac{1}{2} \int EI(x) \left(\frac{\partial^2 w_n(x)}{\partial x^2} \right)^2 dx. \quad (9)$$

Considering periodic boundary conditions, the displacement and its second derivative between the nth and the $(n+1)$th unit-cells should satisfy the following relationship

$$w_{n+1}(x+a) = e^{jka} w_n(x), \quad (10)$$

$$w''_{n+1}(x+a) = e^{jka} w''_n(x), \quad (11)$$

where k is the wave vector and a is the lattice constant.

By substituting Eqs. (10) and (11) into Eq. (9), the relationship $L_{n+1} = e^{2jka} L_n$ is obtained. Similarly, the Lagrangian of any $(n+q)$th unit-cell is obtained by $L_{n+q} = e^{2qjka} L_n$ with q being any integer. Thus, Eq. (8) can be rewritten as

$$L = \sum_{n=-\infty}^{+\infty} L_n = L_n \sum_{q=-\infty}^{+\infty} e^{2qjka}. \quad (12)$$

Therefore, the extremalization of the Hamiltonian function of the entire infinite system can mathematically be expressed in terms of the Lagrangians of one unit-cell as follows

$$\frac{d}{dt} \left(\frac{\partial L_n}{\partial \dot{a}_{i,s}(t)} \right) - \frac{\partial L_n}{\partial a_{i,s}(t)} = 0. \quad (13)$$

In other words, solving the Lagrange's equations of one-unit cell leads to the result for the whole system. Meanwhile, this set of Lagrange's equations has a very similar form as the one established in part II for one ABH element. The only difference is that this single unit-cell is boundary free with artificial spring stiffnesses K and Q being set to zero, and

satisfies the periodic boundary conditions in terms of displacement, rotation angle, bending moment, and shear force as follows:

$$w_n(a) = e^{jka}w_n(0), \tag{14}$$

$$w_n'(a) = e^{jka}w_n'(0), \tag{15}$$

$$w_n''(a) = e^{jka}w_n''(0), \tag{16}$$

$$w_n'''(a) = -e^{jka}w_n'''(0). \tag{17}$$

The displacement w can be rewritten as $w(x,t) = \sum_{i=0}^{m}\sum_{s} a_{i,s}(t)\varphi_{i,s}(x) = \sum_{i=1}^{n} a_i\varphi_i(x)$. Taking the periodic boundary condition Eq. (14) into account, one can get

$$\sum_{i=1}^{n}\left(\varphi_i(a) - e^{jka}\varphi_i(0)\right)a_i = 0, \tag{18}$$

$$a_n = \sum_{i=1}^{n-1}\lambda_i a_i, \tag{19}$$

with $\lambda_i^m = \frac{A_i^m}{A_n^m}$ and $A_i^m = \varphi_i^m(a) - e^{jka}\varphi_i^m(0)$. Here, the superscript m denotes the derivative order. The displacement can then be re-expressed as

$$w(x,t) = \sum_{i=1}^{n-1}[\varphi_i(x) - \lambda_i\varphi_n(x)]a_i. \tag{20}$$

Considering additional periodic boundary condition Eq. (15), we can get a_{n-1} and the displacement similarly as

$$a_{n-1} = \sum_{i=1}^{n-2}\left(\frac{\lambda_i' - \lambda_i}{-\lambda_{n-1}' + \lambda_{n-1}}\right)a_i, \tag{21}$$

$$w(x,t) = \sum_{i=1}^{n-2}\left\{\varphi_i(x) + \frac{\lambda_i' - \lambda_i}{-\lambda_{n-1}' + \lambda_{n-1}}\varphi_{n-1}(x)\right. $$
$$\left. + \left[\frac{\lambda_i' - \lambda_i}{\lambda_{n-1}' - \lambda_{n-1}}\lambda_{n-1} - \lambda_i\right]\varphi_n(x)\right\}a_i. \tag{22}$$

With further consideration of the other two periodic boundary conditions, Eqs. (16) and (17), the displacement can be accordingly rewritten as detailed in the Appendix. Submitting the displacement expression into Eq. (13), one can get a matrix equation similar to Eq. (7) in the harmonic regime. For each given value of wave vector k, the corresponding eigen-frequencies can be determined from the matrix equation. This allows us to obtain the dispersion curves of the lattice, from which band characteristics of the structure can be revealed.

IV. COMPARISONS BETWEEN THE INFINITE AND FINITE PERIODIC STRUCTURES

A. Model verification and mechanism exploration

Using the same material and ABH parameters as before, infinite periodic structures are investigated hereafter to explain the physical phenomena previously observed on the finite structures with multiple ABHs.

In Fig. 6, we compare the dispersion curves obtained using the present model under different periodic boundary conditions with those from the FEM results using COMSOL Multiphysics. For the FEM, one 2-D unit-cell is developed with a sufficient mesh and the Floquet periodic boundary condition is imposed at the edges of the unit-cell. A reduced frequency f_R, defined as $f_R = fa/c$, is also introduced as a reference, with c being the wave velocity of the uniform beam (with a length of a). As can be seen, the results from the present model with two periodic boundary conditions, displacement w and rotation angle w', match very well with the results from the FEM especially in the mid-low frequency range. The differences at the high frequencies are mainly attributable to neglect of the shear and torsional effect in the present method. Note that using the additional periodic boundary conditions of w'' and w''' brings barely noticeable changes to the results. This indicates that the two periodic boundary conditions on the displacement and rotation angle are sufficient to describe the structural periodicity as well as the band structures. Meanwhile, five band gaps are shown to exist below 30 kHz. The first three are relatively flat, showing typical characteristics of locally resonant band gaps. The bandwidth versus the central frequency of the band, i.e., $\frac{f_{R\_upper} - f_{R\_lower}}{(f_{R\_upper} + f_{R\_lower})/2}$, is used to describe the relative bandwidth. The relative bandwidths of the first three band gaps are 1.38, 1.21, and 0.35, respectively, which are very broad compared with the conventional locally resonant bandwidths.

The observed phenomenon can be explained by the theory elaborated in Mead.[34] In symmetric structures, all coupling coordinates between any two neighboring unit-cells can be divided into two types: the first type (type I coordinate) has the same sign and magnitudes, whereas the second (type II coordinate) has opposite signs and equal magnitudes for a symmetric vibration mode. It was theoretically proven that the bounding frequencies of the passbands can be identified with the natural frequencies of a single periodic element with two classes of boundary conditions – type I coordinate locked and type II free, or oppositely, type I free and type II locked. Specifically, the displacement and the rotational
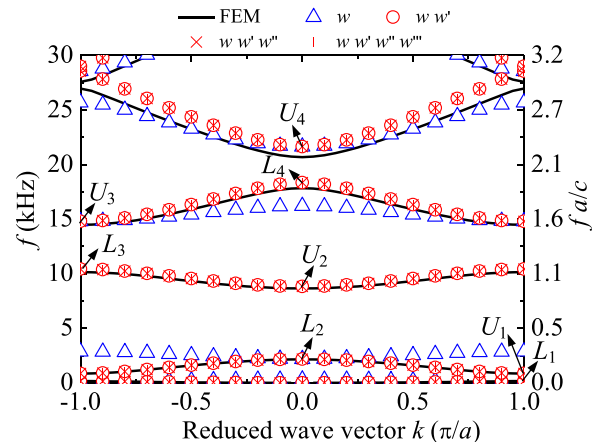

FIG. 6. Dispersion curves. Comparison between the results from the present infinite periodic model with different periodic boundary conditions and from the FEM. $f_R = fa/c$ is the reduced frequency with c being the wave velocity of the uniform beam having length a.
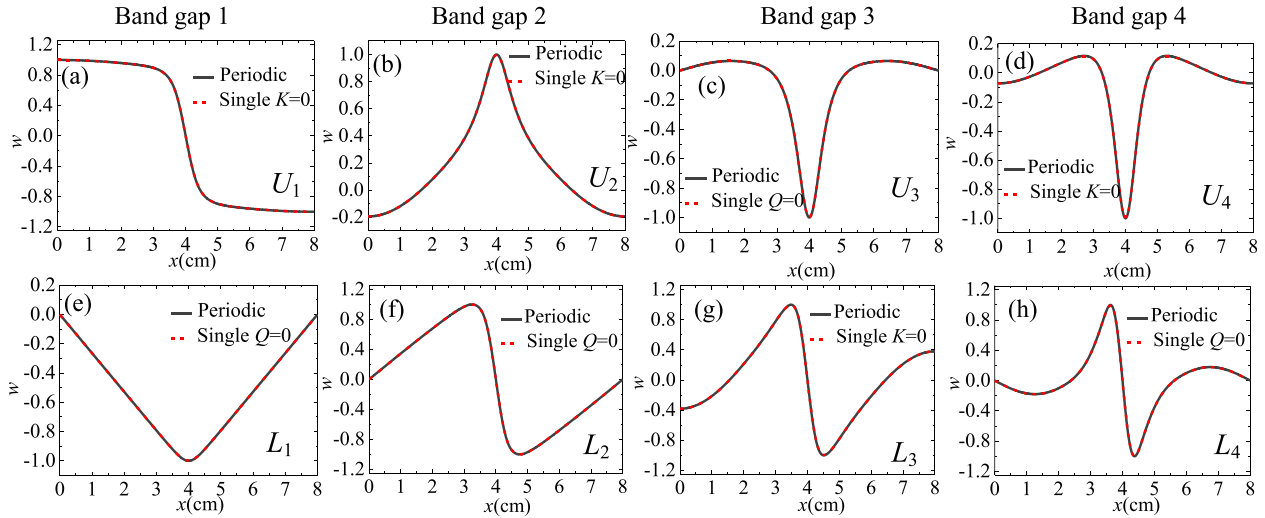
FIG. 7. Mode shape comparisons between the bounding frequencies of the band gaps and the resonant frequencies of a single element: the upper row relates to the upper bounding frequencies, while the lower row is the lower bounding frequencies of each band gap.

slope belong to I and II coordinates, respectively. Therefore, in the present case, the aforementioned periodic boundary condition in terms of displacement and rotational slope can fully determine the band structures. When predicting the band gaps using one periodic element, this corresponds to simply supported or sliding-sliding boundary conditions, which can be achieved by setting K or Q to zero.

The above analyses can be further validated by comparing the mode shapes between the bounding frequencies of the band gaps (labeled in Fig. 6) and the resonant frequencies of a single element, as shown in Fig. 7. The mode shapes, as well as the resonant frequencies (not shown here), from the single element match perfectly with those of the infinite beam. We highlight that, with the help of the previously developed finite model, one can obtain band structure information by only analyzing a single element rather than the entire infinite periodic structure. This greatly saves calculation time and provides a simple way to predict, and eventually optimize, band structures based on a single element. Looking back at the mode shapes of the unit-cell, vibration mainly concentrates on the ABH part with reduced wavelengths, as shown in Fig. 7. The ABH effect promotes wave accumulation with decreasing structural thickness and, consequently, the wave amplitude is amplified. Ideally, if the thickness of the ABH approaches zero, no wave will be reflected back, such that an ABH element could be an ideal local resonator containing multiple localized frequencies for the full frequency band. The inevitable truncation thickness however generates wave reflections, albeit weak in practice, partly impairing local resonance effects. When the ABH part dominates the vibration of the unit-cell while the uniform part is weakly activated, locally resonant modes and band gaps appear, exemplified by the first and third modes and band gaps shown in Figs. 7 and 6. Conventional methods to achieve locally resonant band gaps use single-degree-of-freedom spring mass resonators, which are only effective near their resonant frequencies within a relatively narrow band gap. In the present case, however, the ABH part acts as a continuous local resonator with multiple degrees of freedom, thus generating multiple broad locally resonant band gaps. The local resonance is gradually weakened when the uniform part is activated with increasing frequency, as shown in the mode shape of band gap 4 in Fig. 7.

To demonstrate the correlation between the behavior of the finite structure and that of the infinite periodic structure, the dispersion curves of the infinite periodic beam and the vibration transmission of the finite beam with three ABHs are re-plotted and compared in Fig. 8. The distribution of the transmission attenuation bands is in good agreement with the band gaps. Moreover, only three ABH elements are needed to create attenuation bands, as a result of the dominant role played by the local resonant mechanism of the
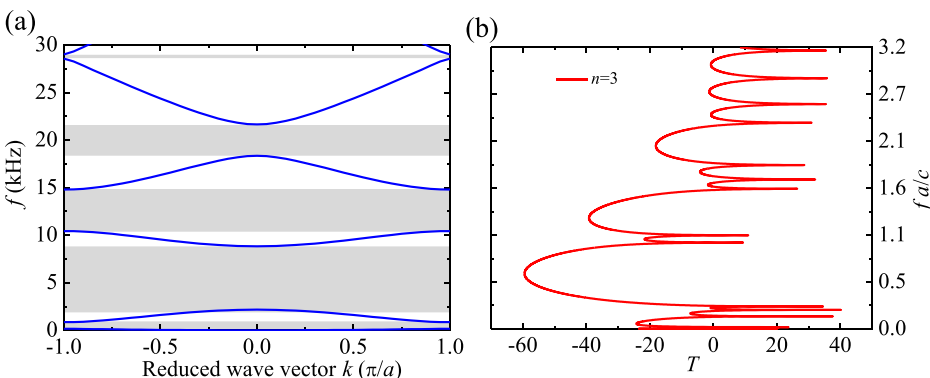

FIG. 8. (a) Dispersion curves of the infinite periodic beam; (b) transmission of finite beam with three ABH elements.
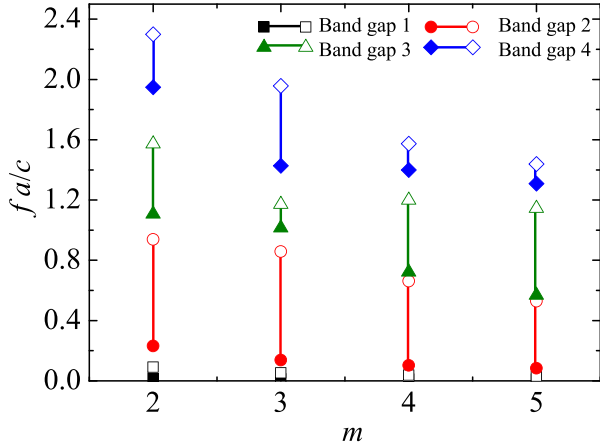
FIG. 9. Effect of the power index m on the band gaps: the solid symbols denote the lower boundaries of the band gaps, the open symbols denote the upper boundaries, and the solid line between symbols indicates the bandwidth.

FIG. 10. Effect of the truncation thickness h_0 on the band gaps: the solid symbols denote the lower boundaries of band gaps, the open symbols denote the upper boundaries, and the solid line between symbols indicates the bandwidth, while the blank means the passband.

ABH elements. Contrary to Bragg scattering, which strongly depends on the periodicity of the elements, the locally resonant effect relies on the locally resonant characteristics of the unit-cells more than the periodicity.[24] Consequently, the attenuation bands obtained here are also due to the locally resonant characteristics of the unit cells rather than the periodicity of the elements in the beam structures.

B. Parametric analyses

In this section, we investigate effects of the geometrical parameters of the ABH taper, such as the power index m and the truncation thickness h_0, on the band gaps.

Fig. 9 illustrates the first four band gaps for different power indices m. As one can see, increasing m would decrease the lower and upper boundary of band gaps overall. Meanwhile, in most cases, the bandwidth at low frequencies also increases with larger m. The passband also becomes narrower with increasing m, which leads to flatter band gaps on the dispersion curves and better local resonant characteristics. This can be understood in light of the positive effect of m on the ABH effect. It is relevant to note that, with an excessively large m, the smoothness criteria would no longer be satisfied,[8,35] and would possibly generate wave scattering, impairing the ABH effect. As a result, the local resonance effect may also be weakened and so would the locally resonant band gaps.
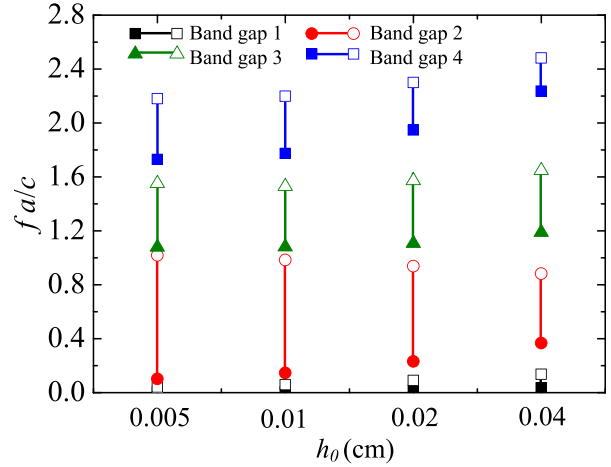
Fig. 10 illustrates how the truncation thickness h_0 affects the band gaps. Nearly every band gap becomes wider as h_0 decreases, along with a significant reduction in the passbands. This can be directly attributed to the enhanced ABH effect. If further decreases in the truncation thickness h_0 are allowed, even broader band gaps can theoretically be achieved, although the extremely thin thickness is most likely prohibited by manufacturing difficulties and ensuing structural strength problems.

As an example, consider infinite periodic and finite periodic beams, both containing identical ABH elements with $m = 2$ and $h_0 = 0.005$ cm. The dispersion curves of the infinite beam and the transmission of the finite beams with different ABH elements are compared in Fig. 11. For the infinite beam, extremely broad band gaps can be observed, covering nearly the entire frequency band below 20 kHz with only a few narrow passbands. For the finite beams, the corresponding attenuation bands are also observed. It is interesting to note that transmission attenuation gaps start to appear with only one ABH element because of the locally resonant effect. With three periodic elements, the transmission can be as low as -120 dB, leading to a significant broadband and low frequency vibration attenuation by using only a few elements without any add-on resonators or creating geometrical or material discontinuous like conventional lattices. It is relevant
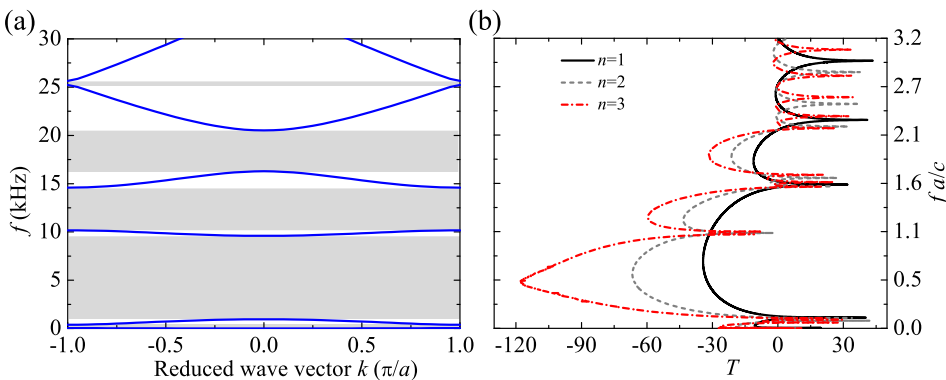

FIG. 11. (a) Dispersion curves of an infinite periodic beam, and (b) the corresponding transmission of finite beams with different ABH elements for $m = 2$ and $h_0 = 0.005$.

to mention that this happens because of the sequential wave travel path across the ABH cells in 1-D beam structures.

V. CONCLUSIONS

In this paper, an Euler-Bernoulli beam containing multiple ABHs is studied based on a wavelet-decomposed energy method. Broadband attenuation bands and wave suppression phenomena are observed at relatively low frequencies below the so-called characteristic frequency. To explain the underlying physical phenomena, the wavelet-decomposed energy model is further extended to investigate infinite structures with ABH unit cells. The periodic boundary conditions in terms of displacement and rotational slope are shown to be sufficient to describe the structural periodicity and the corresponding band structures numerically and analytically. Using this model, the frequency bounds of the band gaps can be predicted solely based on the resonant frequencies of a single cell with simply supported or sliding-sliding boundary conditions. Therefore, the band structures can be easily obtained using the proposed finite model without calculating the dispersion curves of the corresponding infinite structures. Numerical results show that the observed attenuation bands correspond to the band gaps of the corresponding infinite structures with the same ABH elements. Analyses on eigenmodes show that the band gaps can be attributed to the local resonances of the ABH elements as a result of the ABH effect. Therefore, increasing the taper power index m within the smoothness criteria, or reducing the truncation thickness h_0 within the allowable practical range, would help generate broader and lower-frequency band gaps. For 1D structures of finite size, a significant wave attenuation phenomenon occurs because of the enhanced locally resonant effect of multiple ABH cells. Because of the unique wave propagation feature of the 1D structures, waves pass through each ABH cell, collectively forming a more efficient broadband absorber as long as the ABH cell is cut-on to be effective, even at a relatively low frequency.

As for the structure itself, this work proposes a new type of beam structure to achieve broad attenuation bands in the relatively low frequency region. Contrary to the conventional resonant lattices, only a very few ABH elements are needed with no additional resonator attachment or multiple geometric or material discontinuities. These appealing features may offer great potential for applications such as vibration isolators and wave filter designs in beam structures.

As a final remark, because of the remarkable flexibility and unique features offered by wavelets, the proposed wavelet-decomposed energy model is conducive to solving problems with rapid space-varying wavelengths or structures with severe geometric or material inhomogeneity, exemplified by structures embedded with ABH elements. Benefiting from the energy-based and modular feature of the method, the proposed wavelet-decomposed energy method allows flexible handling of other embedded elements required in various vibration control or energy harvesting applications.

APPENDIX: DISPLACEMENT EXPRESSION UNDER PERIODIC BOUNDARY CONDITIONS

Considering the additional boundary condition Eq. (16), we can get

$$a_{n-2} = \sum_{i=1}^{n-3} \lambda\lambda_i a_i,$$

$$w(x,t) = \sum_{i=1}^{n-3} \left\{ \begin{array}{l} \varphi_i(x) + \lambda\lambda_i\varphi_{n-2}(x) + \left[\lambda\lambda_i \dfrac{\lambda'_{n-2} - \lambda_{n-2}}{-\lambda'_{n-1} + \lambda_{n-1}} + \dfrac{\lambda'_i - \lambda_i}{-\lambda'_{n-1} + \lambda_{n-1}}\right]\varphi_{n-1}(x) \\[4mm] + \left[\lambda\lambda_i \left[\dfrac{\lambda'_{n-2} - \lambda_{n-2}}{\lambda'_{n-1} - \lambda_{n-1}}\lambda_{n-1} - \lambda_{n-2}\right] + \dfrac{\lambda'_i - \lambda_i}{\lambda'_{n-1} - \lambda_{n-1}}\lambda_{n-1} - \lambda_i\right]\varphi_n(x) \end{array} \right\} a_i,$$

$$\text{where} \quad \lambda\lambda_i = \frac{\dfrac{\lambda''_i - \lambda_i}{\lambda''_{n-1} - \lambda_{n-1}} - \dfrac{\lambda'_i - \lambda_i}{\lambda'_{n-1} - \lambda_{n-1}}}{-\dfrac{\lambda''_{n-2} - \lambda_{n-2}}{\lambda''_{n-1} - \lambda_{n-1}} + \dfrac{\lambda'_{n-2} - \lambda_{n-2}}{\lambda'_{n-1} - \lambda_{n-1}}}.$$

With the additional boundary condition Eq. (17), the displacement can be repressed by

$$a_{n-3} = \sum_{i=1}^{n-4} \beta_i a_i$$

$$w(x,t) = \sum_{i=1}^{n-4} \left\{ \begin{array}{l} \varphi_i(x) + \beta_i \varphi_{n-3}(x) + [\lambda\lambda_i + \beta_i \lambda\lambda_{n-3}]\varphi_{n-2}(x) \\[2mm] + \left[\begin{array}{l} \lambda\lambda_i \dfrac{\lambda'_{n-2}-\lambda_{n-2}}{-\lambda'_{n-1}+\lambda_{n-1}} + \dfrac{\lambda'_i - \lambda_i}{-\lambda'_{n-1}+\lambda_{n-1}} \\[3mm] + \beta_i \left(\lambda\lambda_i \dfrac{\lambda'_{n-2}-\lambda_{n-2}}{-\lambda'_{n-1}+\lambda_{n-1}} + \dfrac{\lambda'_{n-3}-\lambda_{n-3}}{-\lambda'_{n-1}+\lambda_{n-1}} \right) \end{array} \right] \varphi_{n-1}(x) \\[6mm] + \left\{ \begin{array}{l} \lambda\lambda_i \left(\dfrac{\lambda'_{n-2}-\lambda_{n-2}}{\lambda'_{n-1}-\lambda_{n-1}} \lambda_{n-1} - \lambda_{n-2} \right) + \dfrac{\lambda'_i - \lambda_i}{\lambda'_{n-1}-\lambda_{n-1}} \lambda_{n-1} - \lambda_i \\[3mm] + \beta_i \left[\lambda\lambda_{n-3} \left(\dfrac{\lambda'_{n-2}-\lambda_{n-2}}{\lambda'_{n-1}-\lambda_{n-1}} \lambda_{n-1} - \lambda_{n-2} \right) + \dfrac{\lambda'_{n-3}-\lambda_{n-3}}{\lambda'_{n-1}-\lambda_{n-1}} \lambda_{n-1} - \lambda_{n-3} \right] \end{array} \right\} \varphi_n(x) \end{array} \right\} a_i,$$

$$\text{where} \quad \beta_i = \frac{\dfrac{\lambda'''_i - \lambda_i}{\lambda'''_{n-1}-\lambda_{n-1}} + \lambda\lambda_i \dfrac{\lambda'''_{n-2}-\lambda_{n-2}}{\lambda'''_{n-1}-\lambda_{n-1}} - \lambda\lambda_i \dfrac{\lambda'_{n-2}-\lambda_{n-2}}{\lambda'_{n-1}-\lambda_{n-1}} - \dfrac{\lambda'_i - \lambda_i}{\lambda'_{n-1}-\lambda_{n-1}}}{-\dfrac{\lambda'''_{n-3}-\lambda_{n-3}}{\lambda'''_{n-1}-\lambda_{n-1}} - \lambda\lambda_{n-3} \dfrac{\lambda'''_{n-2}-\lambda_{n-2}}{\lambda'''_{n-1}-\lambda_{n-1}} + \lambda\lambda_{n-3} \dfrac{\lambda'_{n-2}-\lambda_{n-2}}{\lambda'_{n-1}-\lambda_{n-1}} + \dfrac{\lambda'_{n-3}-\lambda_{n-3}}{\lambda'_{n-1}-\lambda_{n-1}}}.$$

[1] V. V. Krylov and F. J. B. S. Tilman, J. Sound Vib. **274**, 605 (2004).

[2] V. V. Krylov, Acta Acust. Acust. **90**, 830 (2004).

[3] D. J. O'Boy and V. V. Krylov, J. Sound Vib. **330**, 2220 (2011).

[4] V. V. Krylov, IEEE Trans Ultrason Ferroelectr Freq Control. **61**, 1296 (2014).

[5] V. V. Krylov and R. E. T. B. Winward, J. Sound Vib. **300**, 43 (2007).

[6] D. J. O'Boy, E. P. Bowyer, and V. V. Krylov, J. Acoust. Soc. Am. **129**, 3475 (2011).

[7] E. P. Bowyer and V. V. Krylov, Compos. Struct. **107**, 406 (2014).

[8] M. A. Mironov, Sov. Phys.: Acoust. **34**, 318 (1988).

[9] V. V. Krylov, Sov. Phys.–Tech. Phys. **35**, 137 (1990).

[10] V. B. Georgiev, J. Cuenca, F. Gautier, L. Simon, and V. V. Krylov, J. Sound Vib. **330**, 2497 (2011).

[11] L. L. Tang, L. Cheng, H. L. Ji, and J. H. Qiu, J. Sound Vib. **374**, 172 (2016).

[12] E. P. Bowyer and V. V. Krylov, Structures **6**, 48 (2016).

[13] L. L. Tang and L. Cheng, Appl. Phys. Lett. **109**, 014102 (2016).

[14] L. L. Tang and L. Cheng, J. Sound Vib. **391**, 116 (2017).

[15] J. J. Bayod, J. Sound Vib. **133**, 061003 (2011).

[16] V. Denis, F. Gautier, A. Pelat, and J. Poittevin, J. Sound Vib. **349**, 67 (2015).

[17] W. Huang, H. Ji, J. Qiu, and L. Cheng, J. Vib. Acoust. **138**, 061004 (2016).

[18] P. A. Feurtado and S. C. Conlon, J. Vib. Acoust. **138**, 061002 (2016).

[19] S. C. Conlon, J. B. Fahnline, and F. Semperlotti, J. Acoust. Soc. Am. **137**, 447 (2015).

[20] L. X. Zhao, S. C. Conlon, and F. Semperlotti, Smart Mater. Struct. **23**, 065021 (2014).

[21] L. X. Zhao, S. C. Conlon, and F. Semperlotti, Smart Mater. Struct. **24**, 065039 (2015).

[22] M. S. Kushwaha, P. Halevi, L. Dobrzynski, and B. Djafari-Rouhani, Phys. Rev. Lett. **71**, 2022 (1993).

[23] M. S. Kushwaha and B. Djafari-Rouhani, J. Appl. Phys. **84**, 4677 (1998).

[24] Z. Liu, X. Zhang, Y. Mao, Y. Zhu, Z. Yang, C. Chan, and P. Sheng, Science **289**, 1734 (2000).

[25] J. H. Ma, Z. L. Hou, and B. M. Assouar, J. Appl. Phys. **115**, 093508 (2014).

[26] M. Oudich and M. B. Assouar, J. Appl. Phys. **111**, 014504 (2012).

[27] Y. Achaoui, V. Laude, S. Benchabane, and A. Khelif, J. Appl. Phys. **114**, 104503 (2013).

[28] M. B. Assouar and M. OUdich, Appl. Phys. Lett. **100**, 123506 (2012).

[29] Y. Xiao, B. R. Mace, J. H. W., and X. S. Wen, Phys. Lett. A **375**, 1485 (2011).

[30] D. L. Yu, Y. Z. Liu, G. Wang, H. G. Zhao, and J. Qiu, J. Appl. Phys. **100**, 124901 (2006).

[31] H. F. Zhu and F. Semperlotti, Phys. Rev. B **91**, 104304 (2015).

[32] I. Daubechies, "Ten lectures on wavelets," *CBM-NSF Conference Series in Applied Mathematics* (SIAM, Philadelphia, 1992).

[33] T. Hou and H. Qin, Graphical Models **74**, 221 (2012).

[34] D. J. Mead, J. Sound Vib. **40**, 19 (1975).

[35] P. A. Feurtado, S. C. Conlon, and F. Semperlotti, J. Acoust. Soc. Am. **136**, EL 148 (2014).